Velocity discontinuity propagation model validation using an approximate point source in motion

Christopher J. Bahr

Aeroacoustics Branch, NASA Langley Research Center, Hampton, VA 23681, USA[a]

The classic geometric acoustic solution for propagation through a mean flow velocity discontinuity is evaluated experimentally using an approximate point source in motion. The geometric approximation of the pressure field in both the frequency and time domains is first revisited for arbitrary subsonic flow and source motion along the flow axis. The derivation, computed via the method of stationary phase, shows the expected Doppler behavior of the radiated acoustic field due to the source motion acting in conjunction with the convective amplification effect for a stationary source in flow. The model is validated with a minimally intrusive, approximate point source of heat in the Quiet Flow Facility at the NASA Langley Research Center. Within the limitations of the experiment in this open-jet wind tunnel, data generally show agreement with the model across a range of flow speeds and microphone positions for a broad range of frequencies. Where disagreement between measurement and theory is noted, possible causes are discussed.

[a]christopher.j.bahr@nasa.gov

I. INTRODUCTION

In aeroacoustic wind tunnel testing, acoustic instrumentation is often separated from a given facility's test section flow to minimize measurement contamination by hydrodynamic pressure fluctuations. Many such facilities utilize an open-jet test section arrangement, where microphones are separated from the flow field by a free shear layer.[1] These wind tunnels are never perfect acoustic measurement environments due to the various design decisions required in the tradeoffs between tunnel aerodynamic requirements and acoustic behavior.[2] One of the ways of assessing real tunnel effects is to operate an approximately known acoustic source in the test section and calculate the deviation between measurement and the source's expected behavior in the modeled propagation environment. Any deviation would indicate inaccuracies in the propagation model, limitations in knowledge of the source's characteristics, or both.

Such measurements are usually complicated by the source's installation requirements. Many controllable sources are intrusive and alter the flow field in an active wind tunnel test section. Sources may also have an unknown behavior change once immersed in flow. Recently, attempts have been made to circumvent these limitations by using laser-induced plasmas for facility characterization.[3,4] Such sources are minimally intrusive, can approximate a point source, can be isolated in time to mitigate multipath effects, and have an existing model for their behavior in a mean flow.[5] The shear layer refraction of the acoustic field generated by these sources, which convect with the test section flow, can be analyzed by solving the classic stationary point source refraction problem for a velocity discontinuity[6,7] while incorporating source motion. Note that more general formulations of this model exist that account for a realistic mean velocity distribution in a shear layer.[8,9] However, a velocity discontinuity is often assumed in practice both for computational expedience and to avoid requiring detailed measurements of a facility flow field. Historically, such a simplification has shown a minimal influence on data analysis in open-jet wind tunnels for a broad range of measurement angles,[10] though errors in modeling the shear layer shape may cause more significant problems than the discontinuity assumption.[11]

This work revisits the classic planar shear layer refraction problem by using a laser-induced plasma to expand the operational bandwidth of model validation while minimizing source size and influence on the test section flow. It starts by summarizing the classic geometric acoustic model for refraction at a velocity discontinuity, while accounting for source motion in a mean flow. It then validates the model using experimental data acquired in the Quiet Flow Facility at the NASA Langley Research Center, demonstrating the ability to collapse source characteristics for a laser-induced plasma at a variety of measurement locations and Mach numbers. Conditions where the data and model disagree are identified and discussed to assess limitations in both the test setup and modeling. These analyses can be used to scope the utility of a laser-induced plasma source in future open-jet facility characterization efforts, as well as steer where further work should be focused to improve wind tunnel data modeling and reduction.

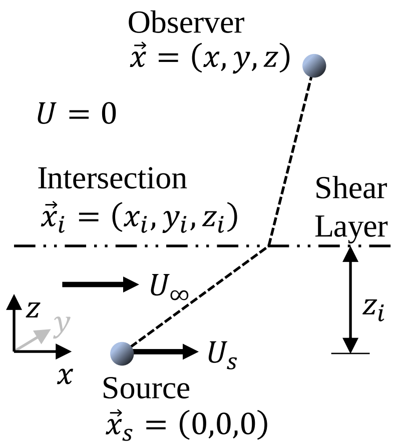

FIG. 1. (Color online) Schematic of the problem of interest at the source initiation time.

II. MODEL DEVELOPMENT

The simplified problem of interest is shown in Fig. 1. Here, the bounding shear layer is approximated as an infinitely thin velocity discontinuity defined as a surface of constant z in the three-dimensional problem domain. The source, located at the origin at time $t = 0$, is assumed to move at a speed of U_s in the x-direction. A mean flow is present in the x-direction with speed U_∞. Both U_s and U_∞ are assumed to be subsonic. The isentropic speed of sound, c_∞, is assumed to be constant throughout the domain. The shear layer has a constant offset of z_i from the source location and is a boundary between the flow and a quiescent medium. The observer is located in the quiescent region.

A. Problem formulation

This is treated as an interface problem, so the incident acoustic field must first be defined. This field is based on the model given by Rossignol et al.[5] for a point source of heat in a unidirectional mean flow, which can be stated as

$$\frac{1}{c_\infty^2}\frac{\partial^2 p_I}{\partial t^2} + 2\frac{M_\infty}{c_\infty}\frac{\partial^2 p_I}{\partial x \partial t} - \beta^2 \frac{\partial^2 p_I}{\partial x^2} - \frac{\partial^2 p_I}{\partial y^2} - \frac{\partial^2 p_I}{\partial z^2} = \frac{\gamma - 1}{c_\infty^2}\left(\frac{\partial q}{\partial t} + U_\infty \frac{\partial q}{\partial x}\right). \tag{1}$$

Here, p_I is the incident acoustic pressure, q is the heat release per unit volume, c_∞ is the speed of sound, M_∞ is the Mach number defined by the free stream flow speed $U_\infty = M_\infty c_\infty$, $\beta = \sqrt{1 - M_\infty^2}$, and γ is the ratio of specific heats. The heat release function is assumed to have the form of a point source in space moving at speed U_s, $q = q_s(t)\,\delta(x - U_s t)\,\delta(y)\,\delta(z)$ with δ as the Dirac delta function. It is assumed that γ is constant. Note that this formulation is equivalent to that of a point source of mass if $(\gamma - 1)\,c_\infty^{-2}$ on the right-hand side of Eq. (1) is replaced with the mean fluid density ρ_∞ and the appropriate dimensional change is made to the source function q.

A wavenumber decomposition in the x- and y-directions is performed on Eq. (1) using the spatiotemporal Fourier transform, in this work defined for a function g as

$$\hat{g}(\nu_x, \nu_y, z, f) = \iiint_{-\infty}^{\infty} g(x, y, z, t)\, e^{j2\pi(\nu_x x + \nu_y y - f t)} \mathrm{d}x\, \mathrm{d}y\, \mathrm{d}t, \tag{2}$$

with spatial wavenumbers ν_x and ν_y, temporal frequency f, and imaginary unit $j = \sqrt{-1}$. The associated inverse transform is given as

$$g(x, y, z, t) = \iiint_{-\infty}^{\infty} \hat{g}(\nu_x, \nu_y, z, f)\, e^{-j2\pi(\nu_x x + \nu_y y - f t)} \mathrm{d}\nu_x\, \mathrm{d}\nu_y\, \mathrm{d}f. \tag{3}$$

Applying the forward transform to Eq. (1) yields the inhomogeneous ordinary differential equation

$$\frac{\mathrm{d}^2 \hat{p}_I}{\mathrm{d}z^2} + 4\pi^2\left[\nu_\infty^2 \eta_\infty^2 - \nu_x^2 - \nu_y^2\right]\hat{p}_I = -j2\pi f \eta_\infty \frac{\gamma - 1}{c_\infty^2}\hat{q}_s(f\eta_s)\,\delta(z), \tag{4}$$

where ν_∞ is the acoustic wavenumber defined by $f = \nu_\infty c_\infty$ and η_∞ is the index of refraction defined by $\nu_\infty \eta_\infty = \nu_\infty - M_\infty \nu_x$. Index of refraction η_s is defined in the same way using $f\eta_s = f - U_s \nu_x$.

The solution to Eq. (4) consists of

$$\hat{p}_I\left(z > 0\right) = A_+ e^{j2\pi\zeta_\infty z} + B_+ e^{-j2\pi\zeta_\infty z} \tag{5}$$

and

$$\hat{p}_I\left(z < 0\right) = A_- e^{j2\pi\zeta_\infty z} + B_- e^{-j2\pi\zeta_\infty z}, \tag{6}$$

where the substitution $\zeta_\infty^2 = \nu_\infty^2 \eta_\infty^2 - \nu_x^2 - \nu_y^2$ for the z-component of the wave vector is made for brevity. As this incident field is defined for an unbounded medium, $A_+ = B_- = 0$ since only waves propagating away from the source can exist. Pressure must be equal at $z = 0$, so $B_+ = A_-$. The jump condition of the source can be addressed by integrating Eq. (4) from $-\epsilon$ to ϵ across $z = 0$. In the limit of $\epsilon \to 0$, the second term on the left side vanishes since pressure is continuous across the jump. The remaining term on the left (after integration) is expressed as first derivatives of Eqs. (5) and (6). For $z > 0$, this yields $2\zeta_\infty B_+ = f\eta_\infty \left(\gamma - 1\right) c_\infty^{-2} \hat{q}_s \left(f\eta_s\right)$ and

$$\hat{p}_I\left(z > 0\right) = \frac{f\eta_\infty e^{-j2\pi\zeta_\infty z}}{2\zeta_\infty} \frac{\gamma - 1}{c_\infty^2} \hat{q}_s\left(f\eta_s\right). \tag{7}$$

B. Interface transmission

The interface problem can now be evaluated. Two conditions are required to solve for the reflected and transmitted pressure fields, given by

$$\hat{p}_R\left(\nu_x, \nu_y, z, f\right) = R e^{j2\pi\zeta_\infty z} \tag{8}$$

and

$$\hat{p}_T\left(\nu_x, \nu_y, z, f\right) = T e^{-j2\pi\zeta z}, \tag{9}$$

with $\zeta^2 = \nu_\infty^2 - \nu_x^2 - \nu_y^2$. The first condition states that, since the interface is not accelerating in the z-direction, pressure must balance across it. This is expressed as

$$T e^{-j2\pi\zeta z_i} = \frac{f\eta_\infty e^{-j2\pi\zeta_\infty z_i}}{2\zeta_\infty}\frac{\gamma-1}{c_\infty^2}\hat{q}_s\left(f\eta_s\right) + R e^{j2\pi\zeta_\infty z_i}. \tag{10}$$

The second interface condition is a displacement condition, where the interface is treated as a wavy, impermeable stream surface. Miles,[12] Ribner,[13] and Amiet[7] all express this in a reference frame moving along the interface in the direction of the surface wave and at its phase speed, $f/\sqrt{\nu_x^2+\nu_y^2}$. In this reference frame, matching displacement across the interface is equivalent to matching the slope of the velocity vector in the plane defined by the surface-wavevector-tangent and interface-normal components of the wave vector. Note that in the limiting case where flow speeds match across an interface, this simplifies to matching the normal velocity. The tangential velocity component is approximated as the mean speed in the direction of the surface wave vector in this moving reference frame, under the assumption that accounting for the acoustic velocity component contribution is a second-order effect.[13] The normal component is determined from the z-derivative of the acoustic velocity potential, ϕ, so matching slopes across the interface gives

$$\frac{1}{U_\infty \frac{\nu_x}{\sqrt{\nu_x^2+\nu_y^2}} - \frac{f}{\sqrt{\nu_x^2+\nu_y^2}}}\left(\left.\frac{\mathrm{d}\hat{\phi}_I}{\mathrm{d}z}\right|_{z_i} + \left.\frac{\mathrm{d}\hat{\phi}_R}{\mathrm{d}z}\right|_{z_i}\right) = \frac{1}{-\frac{f}{\sqrt{\nu_x^2+\nu_y^2}}}\left.\frac{\mathrm{d}\hat{\phi}_T}{\mathrm{d}z}\right|_{z_i}. \tag{11}$$

The velocity potential when mean flow is present is given by the linearized Euler equation as

$$\rho_\infty\left(\frac{\partial\phi}{\partial t} + U_\infty\frac{\partial\phi}{\partial x}\right) = -p, \tag{12}$$

or in the transformed domain as

$$\hat{\phi} = \frac{j}{2\pi\rho_\infty f\eta_\infty}\hat{p}. \tag{13}$$

When there is no mean flow, the index of refraction term becomes unity. Evaluating Eq. (13) for each pressure field and substituting into Eq. (11) yields the second interface expression in terms of R and T,

$$\frac{\zeta\eta_\infty^2 T e^{-j2\pi\zeta z_i}}{\zeta_\infty} = \frac{f\eta_\infty e^{-j2\pi\zeta_\infty z_i}}{2\zeta_\infty}\frac{\gamma-1}{c_\infty^2}\hat{q}_s\left(f\eta_s\right) - Re^{j2\pi\zeta_\infty z_i}. \tag{14}$$

Equations (10) and (14) can be added to eliminate R. Solving for T and then substituting into Eq. (9) yields

$$\hat{p}_T\left(\nu_x,\nu_y,z,f\right) = \frac{f\eta_\infty e^{-j2\pi[\zeta(z-z_i)+\zeta_\infty z_i]}}{\eta_\infty^2\zeta+\zeta_\infty}\frac{\gamma-1}{c_\infty^2}\hat{q}_s\left(f\eta_s\right). \tag{15}$$

C. Approximate spatial solution

The wavenumber transform must now be inverted to recover the frequency-domain pressure for a given location in space. This takes the form of

$$\tilde{p}_T\left(x,y,z,f\right) = \iint_{-\infty}^{\infty}\frac{f\eta_\infty e^{-j2\pi[\nu_x x+\nu_y y+\zeta(z-z_i)+\zeta_\infty z_i]}}{\eta_\infty^2\zeta+\zeta_\infty}\frac{\gamma-1}{c_\infty^2}\hat{q}_s\left(f\eta_s\right)\mathrm{d}\nu_x\mathrm{d}\nu_y. \tag{16}$$

An approximate solution to this type of integral can be computed using the method of stationary phase,[14] given in two dimensions as

$$\iint_{-\infty}^{\infty}\Psi\left(\nu_x,\nu_y\right)e^{jk\Phi(\nu_x,\nu_y)}\mathrm{d}\nu_x\mathrm{d}\nu_y \simeq \frac{2\pi}{k}\sum_{\nabla_{\nu_x,\nu_y}\Phi=0} e^{j\frac{\pi}{4}\operatorname{sgn}\mathrm{H}(\Phi)|_0}\frac{\Psi|_0 e^{jk\Phi|_0}}{\sqrt{|\det\mathrm{H}\left(\Phi\right)|_0|}}, \tag{17}$$

where Ψ is the magnitude function, Φ is the real-valued phase function that drives the oscillations of the complex exponential, and $k \gg 1$ is a scale parameter for Φ. This geometric acoustic approximation is summed over all stationary points $(\nu_{x,0}, \nu_{y,0})$ that satisfy $\nabla_{\nu_x,\nu_y}\Phi = 0$. $\mathrm{H}(\Phi)|_0$ is the Hessian matrix of Φ evaluated at a stationary point. Operators det and sgn represent the matrix determinant and matrix signature, where the signature is the difference between the number of positive and negative eigenvalues of the matrix.[15] For this problem, defining $r = \sqrt{x^2 + y^2 + z^2}$ as the distance between the source and observer, $k = 2\pi\nu_\infty r$,

$$\Psi(\nu_x, \nu_y) = \frac{f\eta_\infty}{\eta_\infty^2\zeta + \zeta_\infty}\frac{\gamma - 1}{c_\infty^2}\hat{q}_s(f\eta_s), \tag{18}$$

and, defining coordinate system $(x', y', z') = (x - x_i, y - y_i, z - z_i)$ with the origin at the shear layer intersection point in Fig. 1 and $r' = \sqrt{x'^2 + y'^2 + z'^2}$,

$$\Phi(\nu_x, \nu_y) = -\frac{1}{\nu_\infty r}\left(\nu_x x' + \nu_y y' + \zeta z' + \nu_x x_i + \nu_y y_i + \zeta_\infty z_i\right). \tag{19}$$

There is one stationary point that satisfies $\nabla_{\nu_x,\nu_y}\Phi = 0$ for a wave propagating in the positive z-direction, and its value depends on the intersection location (x_i, y_i, z_i) of the acoustic ray path with the shear layer. Various expressions are available for relating this location in different coordinate systems, derived by matching the x- and y-components of respective slowness vectors across the interface.[7] The x- and y-coordinates of the intersection can be determined with the problem setup of Fig. 1 by solving the related system of two equations with known source and observer locations,[16]

$$0 = \frac{x_i}{\sigma_i} - \frac{\beta^2 x'}{r'} - M_\infty \tag{20}$$

and

$$0 = \frac{y_i}{\sigma_i} - \frac{y'}{r'}, \tag{21}$$

where $\sigma_i = \sqrt{x_i^2 + \beta^2\left(y_i^2 + z_i^2\right)}$. The stationary point values given in both coordinate systems are then

$$\nu_{x,0} = \nu_\infty \frac{x'}{r'} = \nu_\infty \frac{x_i - M_\infty \sigma_i}{\beta^2 \sigma_i} \tag{22}$$

and

$$\nu_{y,0} = \nu_\infty \frac{y'}{r'} = \nu_\infty \frac{y_i}{\sigma_i}. \tag{23}$$

The resultant expressions for ζ_∞ and ζ are

$$\zeta_{\infty,0} = \nu_\infty \frac{z_i}{\sigma_i} \tag{24}$$

and

$$\zeta_0 = \nu_\infty \frac{z'}{r'}. \tag{25}$$

The determinant of the Hessian matrix and the matrix signature must now be computed. The determinant at the stationary point is given as

$$\det \mathrm{H}\left(\Phi\right)|_0 = \frac{\mathcal{H}^2}{\nu_\infty^4 r^2} = \frac{1}{\nu_\infty^4 r^2} \times \left[\left(\frac{x'^2 + z'^2}{z'^2} r' + \frac{x_i^2 + \beta_\infty^2 z_i^2}{z_i^2} \sigma_i \right) \left(\frac{y'^2 + z'^2}{z'^2} r' + \frac{y_i^2 + z_i^2}{z_i^2} \sigma_i \right) - \left(\frac{x' y'}{z'^2} r' + \frac{x_i y_i}{z_i^2} \sigma_i \right)^2 \right], \tag{26}$$

where $\mathcal{H}^2$ contains all terms within the square brackets and can be shown to be positive. Determining the matrix signature of the Hessian requires calculating its eigenvalues. As the Hessian matrix is real and symmetric, it must have real eigenvalues. As the determinant of this matrix is positive, it can be shown that both eigenvalues are positive, and the matrix signature is 2. The approximate solution for the pressure field in the frequency domain is thus

$$\tilde{p}_T = \frac{j f \eta_{\infty,0} e^{-j2\pi\nu_\infty \left(r' + \frac{\sigma_i - M_\infty x_i}{\beta_\infty^2} \right)}}{\left(\eta_{\infty,0}^2 \frac{z'}{r'} + \frac{z_i}{\sigma_i} \right) \mathcal{H}} \frac{\gamma - 1}{c_\infty^2} \tilde{q}_s \left(f \eta_{s,0} \right), \tag{27}$$

where

$$\eta_{\infty,0} = 1 - M_\infty \frac{x'}{r'} \tag{28}$$

and

$$\eta_{s,0} = 1 - M_s \frac{x'}{r'}. \tag{29}$$

This can now be brought to the time domain using the inverse Fourier transform, giving

$$p_T = \frac{\eta_{\infty,0}}{2\pi \left(\eta_{\infty,0}^2 \frac{z'}{r'} + \frac{z_i}{\sigma_i}\right) \mathcal{H}} \frac{\gamma - 1}{c_\infty^2} \int_{-\infty}^{\infty} j2\pi f \tilde{q}_s \left(f \eta_{s,0}\right) e^{j2\pi f \left(t - \frac{r'}{c_\infty} - \frac{\sigma_i - M_\infty x_i}{c_\infty \beta_\infty^2}\right)} \mathrm{d}f. \tag{30}$$

Here, 2π has been included in both the numerator and denominator to make clear that a time derivative will be present in the solution. Recognizing that the source function is given in terms of Doppler-shifted frequency, a change of variables is required. Defining $f = f_s/\eta_{s,0}$, $\mathrm{d}f = \mathrm{d}f_s/\eta_{s,0}$, and emission time

$$\tau = \frac{1}{\eta_{s,0}} \left(t - \frac{r'}{c_\infty} - \frac{\sigma_i - M_\infty x_i}{c_\infty \beta_\infty^2}\right) \tag{31}$$

allows

$$p_T = \frac{\eta_{\infty,0}}{2\pi \left(\eta_{\infty,0}^2 \frac{z'}{r'} + \frac{z_i}{\sigma_i}\right) \mathcal{H}} \frac{1}{\eta_{s,0}^2} \frac{\gamma - 1}{c_\infty^2} \int_{-\infty}^{\infty} j2\pi f_s \tilde{q}_s \left(f_s\right) e^{j2\pi f_s \tau} \mathrm{d}f_s. \tag{32}$$

This yields the time domain solution

$$p_T \left(x, y, z, t\right) = \frac{\eta_{\infty,0}}{2\pi \left(\eta_{\infty,0}^2 \frac{z'}{r'} + \frac{z_i}{\sigma_i}\right) \mathcal{H}} \frac{1}{\eta_{s,0}^2} \frac{\gamma - 1}{c_\infty^2} \frac{\mathrm{d}q_s \left(\tau\right)}{\mathrm{d}\tau}. \tag{33}$$

Here, both the source motion and mean flow contribute to the directivity of the acoustic field, with some term cancellation in the limiting case of $U_s = U_\infty$.

III. MODEL VALIDATION

The classic model rederived in the previous section is now evaluated using data acquired in the NASA Langley Quiet Flow Facility (QFF). The QFF is an aeroacoustic wind tunnel equipped with a 2- by 3-foot rectangular nozzle. The test section is usually bounded by hard walls on the 2-foot sides and free shear layers on the 3-foot sides. It has a nominal maximum test section Mach number of 0.17.

A. Test configuration

For this test, the laser-induced plasma source was generated using an Nd:YAG (Gemini PIV 120 mJ, 532 nm, 3–5 nsec pulse width) system operating at six pulses per second. The laser was focused to a point in space using a set of 3-inch diameter achromatic expansion, collimating, and focusing lenses. When used in this fashion, such lasers generate a plasma-induced shockwave[17] that quickly decays to a linear acoustic wave and acts as a minimally intrusive acoustic source moving with the flow.[5] It is considered minimally intrusive rather than nonintrusive as, near the source, enough energy is imparted to the fluid to allow for active flow control.[18] It is treated as an approximate rather than true point source as the most energetic band of its spectrum occurs at frequencies where the acoustic wavelength is on the order of the effective source size of several millimeters. However, for the overall measurement dimensions in a typical wind tunnel, noncompactness effects are considered negligible.

The acoustic emissions from the source were measured by a set of microphones covering a partial spherical wedge of radius 66 inches with an origin at the source location. This coverage, located entirely outside of the test section flow, consisted of two arcs of seven microphones each. The microphones in each arc were separated by 15° increments in polar angle, defined from the flow direction. The arcs were separated by 30° in azimuth angle, defined from the modeled shear layer surface normal. Schematics of the two microphone arcs are shown in Fig. 2. An additional microphone, not shown in the figure, was installed on a tripod at $(90°, 15°)$. A reference microphone was also installed in one of the test section sidewalls. A photograph of the overall installation is shown in Fig. 3. In this photograph, the laser system is installed behind the right sidewall. The beam passed through a glass panel and was focused at the center of the test section. The reference microphone was in the left sidewall, with an angular location of $(78°, -90°)$. While close to the beam axis, this microphone was not directly illuminated by laser light. For this test, all acoustic instrumentation consisted of Brüel & Kjær type 4138 1/8-inch pressure-field microphones powered by type 2690 NEXUS conditioning amplifiers with extended upper frequency limits of 140 kHz. The protective gridcaps on the microphones were removed to reduce installation effects on the measured microphone signals. The in-wall reference microphone was flush mounted in the sidewall using a 3D-printed sleeve.

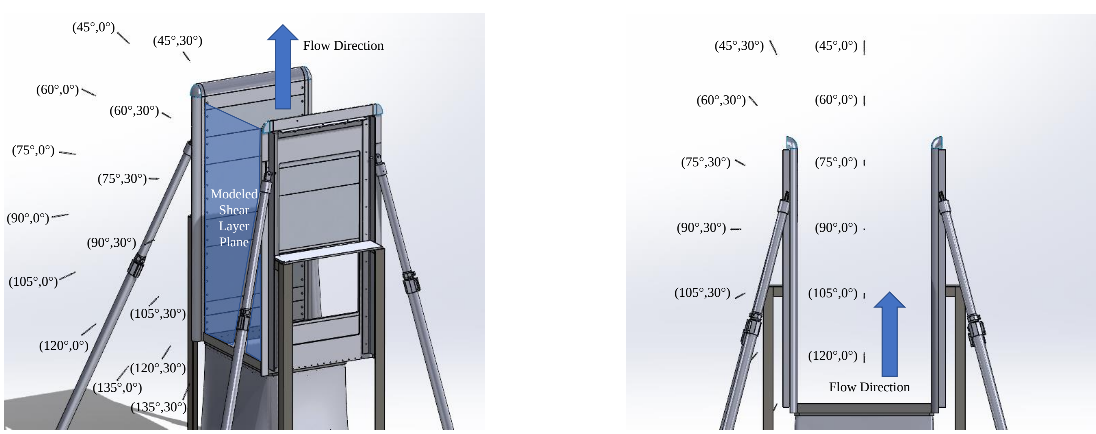

(a) (b)

FIG. 2. (Color online) Microphone arcs used in acoustic measurements, 2(a) isometric and 2(b) side view. Each microphone position is labeled as (polar,azimuth).

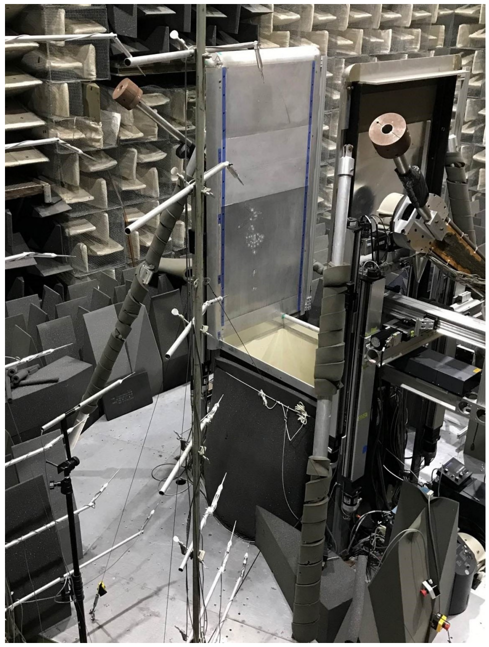

FIG. 3. (Color online) Photograph of facility measurement setup [Source: NASA].

B. Acquisition and processing

Data were aquired using National Instruments PXIe-4480 cards set to a sampling rate of 1.25 MSamples/sec. All microphones, along with lamp and q-switch signals from the laser and the output from a reference photodetector, were simultaneously recorded for 30 sec, acquiring a total of 180 plasma events per test condition. No analog filter was applied beyond the antialiasing filter for the data system, but a 900 Hz zero-phase digital highpass filter was applied to all recorded microphone data prior to processing.

The records were subdivided into individual blocks of 20480 samples for each plasma event with each block starting 25 samples prior to the laser firing. The laser firing time was defined as $t = 0$ for each block. This was determined from the q-switch signal and verified with the photodetector. A 200 µsec long 25% Tukey window was applied to each block of data around the initial pulse acoustic waveform to isolate the direct propagation signal. This removed reflections from the facility sidewalls and nozzle edges and reduced the influence of facility background noise. The specific window selection and sizing was empirically found to successfully mitigate secondary signals for most test conditions while being wide enough to accomodate pulse distortion effects caused by propagation through the turbulence of the free shear layer.[19,20] Due to these distortion effects, data were analyzed in terms of energy spectral densities. Background noise spectra, computed using measurement data without a plasma event, were processed in the same way as the data of interest and subtracted from the spectra of interest. These resultant spectra were corrected for atmospheric attenuation,[21] microphone actuator response, and directivity[22] in an attempt to approach the spectra of the undisturbed acoustic field. Atmospheric attenuation and directivity were corrected using the references, while actuator responses for each microphone were measured via electrostatic calibration. From Eq. (27), the resultant corrected spectral density of a microphone measurement, G_{pp}, is related to the spectral density of the heat release function, G_{qq}, by

$$G_{pp}\left(x,y,z,f\right) = \frac{f^2\eta_{\infty,0}^2}{\left(\eta_{\infty,0}^2\frac{z'}{r'}+\frac{z_i}{\sigma_i}\right)^2\mathcal{H}^2}\frac{\left(\gamma-1\right)^2}{c_\infty^4}G_{qq}\left(f\eta_{s,0}\right). \tag{34}$$

This equation was used to compare heat release estimates from each microphone.

If the model and all corrections are accurate, G_{qq} estimates should match across all microphones. Mismatch in G_{qq} estimates would indicate limitations in the propagation model, considered subsequently, or limitations in the source model, for example nonlinear effects and source directionality. Nonlinearity is not evaluated with these measurements, though the pressure waveforms are in the linear propagation regime by the time they arrive at the out-of-flow microphones. Omnidirectionality can be assessed within the limited coverage provided by the microphone arcs.

C. Results and discussion

Example waveforms from the test are shown in Fig. 4. Here, all 180 pulses acquired in a given acquisition are synchronized based on the signal from the laser q-switch and superimposed. As shown in Fig. 4(a), the source shows high repeatability when no flow is present. However, the aforementioned propagation through the turbulence of the test section free shear layer randomizes both the waveform arrival time and shape,[4] as shown in Fig. 4(b). Note that even with no flow, the waveform shape is distorted by the microphone impulse response function and installation effects.[23,24]

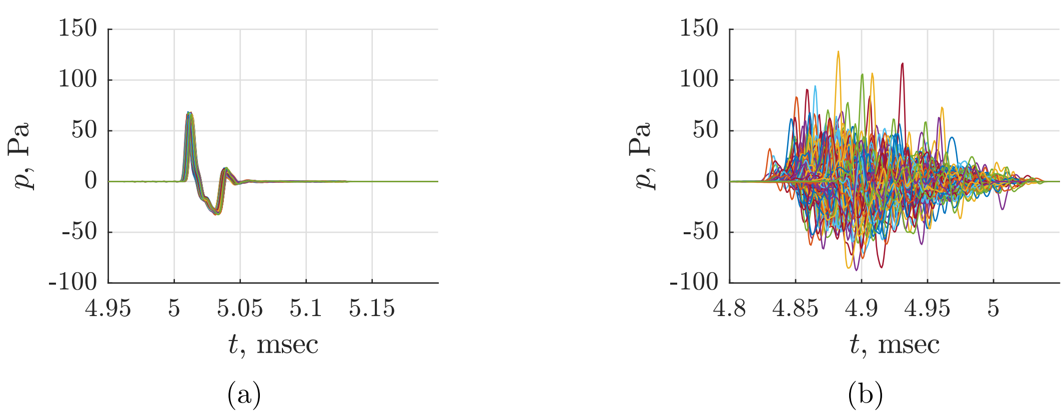

FIG. 4. (Color online) Superimposed plots of 180 sequential, synchronized, gated waveforms for 4(a) no flow and 4(b) Mach 0.17 as measured by the microphone at $(45°, 0°)$.

Energy spectral densities for all microphones with no flow are shown in Fig. 5(a). If all spectral corrections are accurate and the source is an ideal point source, the spectra from the spherical wedge of microphones should overlay each other perfectly for this condition while the reference microphone should have the same spectral shape at a higher level. From the plot, it is clear that the spectral shape of the reference microphone differs from that of the other microphones, particularly in terms of the spacing and width of the secondary and tertiary lobes in the plotted frequency band. As with the waveform shape, these spectral lobes are highly dependent on the instrumentation selection and installation.[23–25] Note that these installation effects are not captured by the correction curves supplied by the instrumentation manufacturer,[22] and further study is warranted if an accurate model of the true source spectrum is desired. It is unclear whether the observed difference between the reference microphone spectrum and other microphone spectra is due to source directivity near the beam axis, said installation effects, or the reference microphone observing nonlinearity, and the test setup does not provide sufficient information to separate these possibilities. As such, in this work, the reference microphone can only be used to track source stability, which was excellent throughout the test duration.

The microphone measurements with no flow are used to construct a source model, $G_{qq,\mathrm{model}}$, plotted in Fig. 5(b). This is the average of the source estimates, G_{qq}, from most of the microphones. The reference microphone is excluded, as are the two microphones at polar angles of 135° and the tripod microphone at an azimuth angle of 15°. The two microphones at 135° are excluded as, without flow, the selected Tukey window cannot fully isolate the acoustic signal of the direct propagation path from that scattered by the test section nozzle edge. Due to changes in propagation time, this issue is mitigated with increasing test section flow speed and these microphones are included in subsequent analyses. The tripod microphone at 15° azimuth appeared to have a bad frequency response function calibration. Data from the tripod microphone are not considered further in this work.

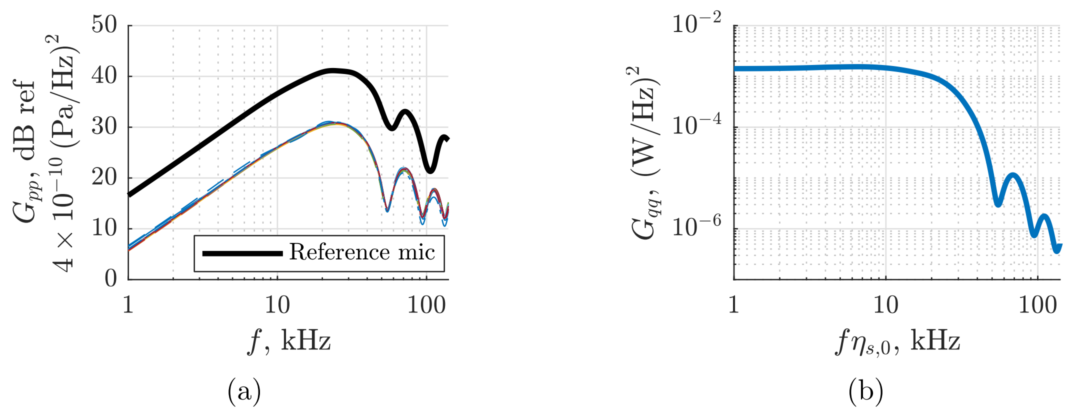

FIG. 5. (Color online) Energy spectral densities for 5(a) all microphones with no flow and 5(b) the resultant model source function $G_{qq,\mathrm{model}}$ after microphone downselection.

Energy spectral densities for all included microphones at all test section speeds are plotted in Fig. 6(a). This overlay of 112 spectra shows that the data with flow share the same spectral shape as those without flow in Fig. 5(a), but misalign in terms of frequency and level. The visual collapse of G_{qq} for all 112 conditions given in Fig. 6(b) shows that, qualitatively, the classic shear layer propagation model holds well across the range of test section speeds and measurement locations. Some low-frequency variability is apparent. This is likely due to reduced signal-to-noise ratios at lower frequencies and higher Mach numbers.

For quantitative evaluation, a decibel-scale deviation function is defined as

$$\Delta_{\mathrm{dB}}\left(f\eta_{s,0}\right) = 10\log_{10}\left(G_{qq}/G_{qq,\mathrm{model}}\right). \tag{35}$$

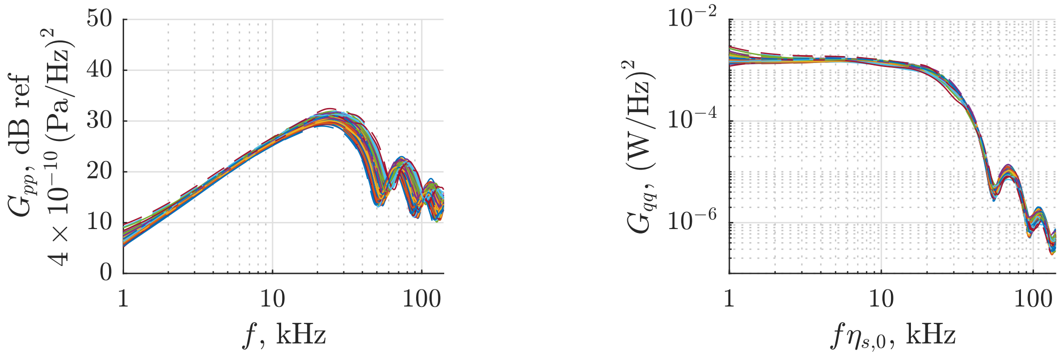

(a) (b)

FIG. 6. (Color online) Energy spectral densities for 6(a) all out-of-flow microphones at all test section speeds and 6(b) the associated source function estimates.

Here, linear interpolation is used to compute deviations where the Doppler-scaled frequencies do not align with the frequency bins of the model. This deviation function is plotted for all microphones, subdivided by test section speed, in Fig. 7.

Broadly speaking, the plots show differing behaviors at low (< 5 kHz), mid (5 –40 kHz), and high (> 40 kHz) frequencies. At low frequencies and low Mach numbers, the microphone at $(135°, 30°)$ shows more deviation than the other microphones. This is due to the aforementioned scattering from the test section nozzle edge and disappears with increasing Mach number. At higher Mach numbers, deviation in the low frequency range increases, moreso for the downstream microphones at lower polar angles. This is caused by contamination by facility background noise, which due to the poor signal-to-noise ratio in this frequency range cannot be completely mitigated by the gating effect of the Tukey window or by background noise subtraction.

At high frequencies, the deviation function shows sharp peaks and troughs. These are due to the misalignment of the troughs between spectral lobes, as the Doppler correction does not completely collapse data along the frequency axis. This behavior is not observed in a similar calculation performed on the reference microphone in the test section wall (not shown), and suggests that there is some unknown interplay between uncertainty in the shear layer state and the specifics of the installation effects of the microphone on the recorded acoustic signal. Since neither of these issues can be addressed with the data at hand, further quantitative evaluation of the high frequency range is not possible.

The mid-frequency data show very little deviation ($\pm \sim 0.25$ dB) at lower Mach numbers, indicating that the combined source and propagation models are in strong agreement with the measured data. However, starting at Mach 0.09 the microphone data at the 45° polar angle begin to diverge from the rest of the measurements. This divergence irregularly increases with Mach number, and by Mach 0.17 several other microphones show this behavior. Generally, these are downstream, suggesting a directivity influence on the deviation function.

This directivity effect is briefly evaluated in Fig. 8, where the deviation function is plotted for all Mach numbers at three microphones on the 0° azimuth polar arc. For reasons previously identified, only the mid-frequency data are discussed. In general, the upstream and centered microphones show strong model agreement in this frequency band, while the downstream microphone shows more deviation with increasing Mach number. The test geometry might indicate that this is an issue related to shear layer thickness. However, for this maximum Mach number and polar angle range, previous work suggests deviation due to shear layer thickness should not be significant.[7,11] The measurement locations are well outside the expected zone of silence,[8] so related effects are unlikely. While shear layer curva-

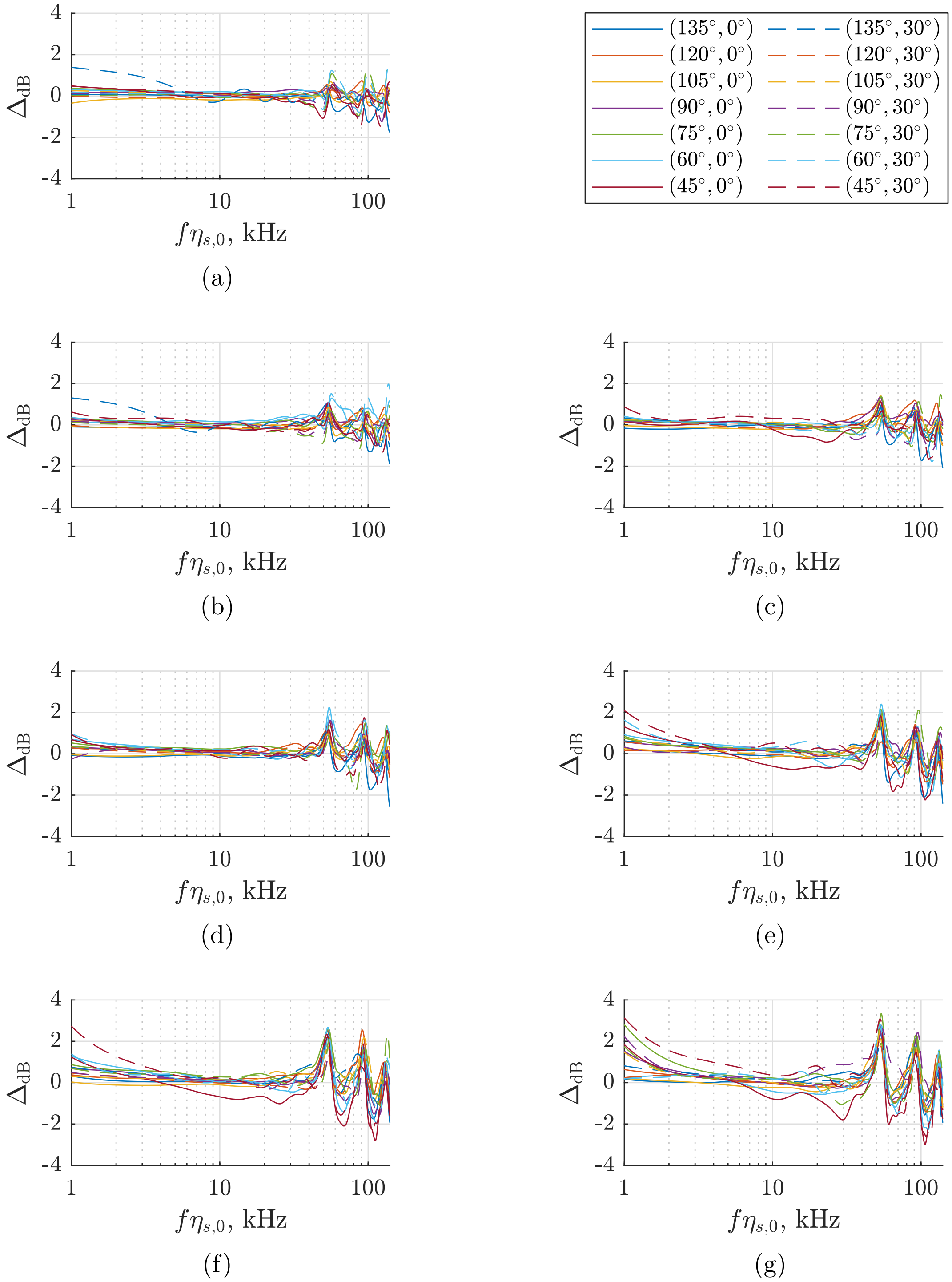

FIG. 7. (Color online) Deviations from model predictions for 7(a) Mach 0.05, 7(b) Mach 0.07, 7(c) Mach 0.09, 7(d) Mach 0.11, 7(e) Mach 0.13, 7(f) Mach 0.15, and 7(g) Mach 0.17.

ture has been demonstrated to have a more significant effect on downstream measurements when applying a parallel flow model,[11] previous work in the QFF has never shown signs of flow curvature during empty test section operations.

One possibility warranting further investigation is the influence of propagation through the turbulence of the free shear layer. Previous work has shown that strong turbulence scattering effects are present in open-jet operations of the QFF, that they increase with increasing test section Mach number, and that they are more significant for downstream measurement locations.[4] This would certainly account for the observed behavior of the deviation function, aside from the jump in the result for the 135° microphone at Mach 0.17 in Fig. 8(a). Insufficient data are available to assess this jump further.

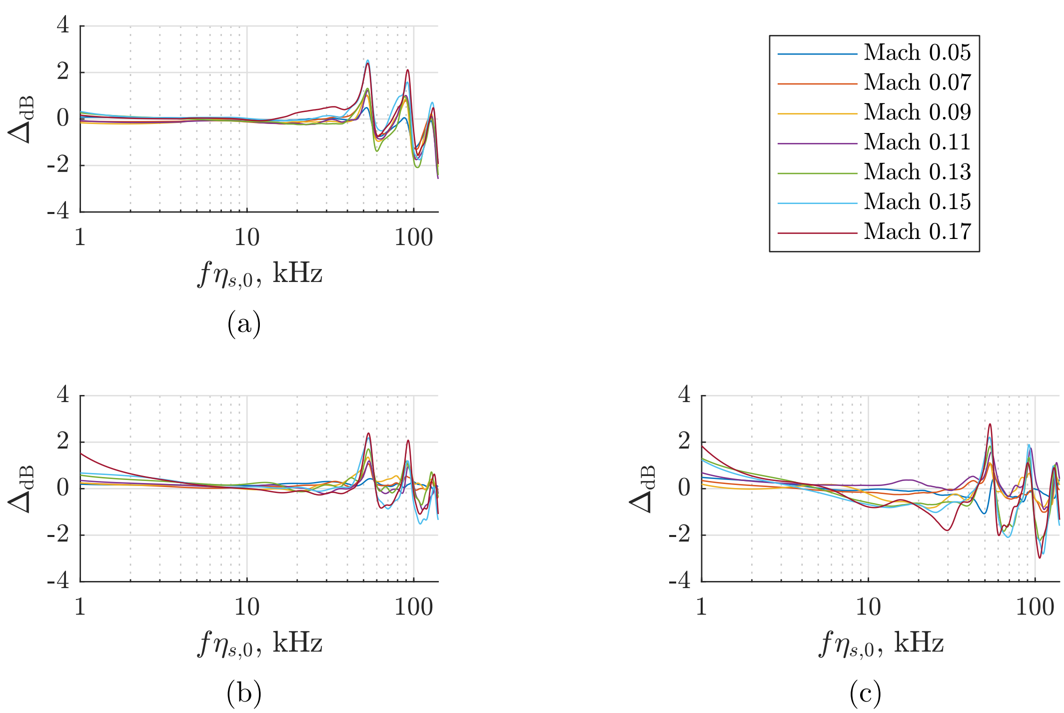

FIG. 8. (Color online) Deviations from model predictions for 8(a) $(135°, 0°)$, 8(b) $(90°, 0°)$, and 8(c) $(45°, 0°)$.

IV. SUMMARY & CONCLUSIONS

A classic model for sound wave refraction at a velocity discontinuity between a moving medium and a quiescent one is revisited using an approximate point source in motion. The source is known to act as one of heat release, making it relatable to a mass source. The approximate solution from classic derivations is restated using the traditional geometric acoustic approximation and the method of stationary phase. Both source motion and mean flow contribute to the directivity of the radiated acoustic field. The model for the pressure field is validated using an Nd:YAG laser focused to a point in the test section of a subsonic, open-jet test section wind tunnel. This focused beam generates a laser-induced plasma. The resultant acoustic source has unique properties that enable detailed characterization of the aeroacoustic wind tunnel environment, in this case isolating the effects of propagation through the free shear layer.

Pressure measurements at a variety of microphone locations and test section speeds are evaluated using the model by extracting the equivalent heat release function. Qualitatively, the data show good collapse for both amplitude and frequency among all of the out-of-flow microphones. Data without flow are used to compute a quantitative metric to evaluate data with flow. This metric is used to identify facility background noise and instrumentation installation effects as likely limitations in the current model validation test setup for low and high frequencies. At mid-range frequencies, where factors such as these do not appear to interfere with the results, good agreement with the source and propagation model is generally seen. Deviation from the model at downstream locations is hypothesized to be due to the effects of propagation through the turbulence in the free shear layer. If this hypothesis is true, it suggests that the mean flow effects on propagation and associated wind tunnel data corrections are well understood. Further improvement on wind tunnel data analysis, when a shear layer is approximately planar, requires accounting for random media propagation in any models and related corrections. Future work should be planned accordingly.

That said, the good agreement between the data and model at mid-range frequencies suggests that this source and the associated deviation metric can be used to assess propagation in larger facilities with more complicated propagation characteristics, assuming sufficiently high signal-to-noise ratios for the source. Often the same propagation assumptions (planar shear layer, no reverberance) are applied in large tests with complex aerodynamic flows. Using a laser-induced plasma source in such experiments and computing deviation from the presented model can illustrate where and by how much the conventional assumptions fail due to, for example, mean flow/shear layer curvature or turbulence effects. Additionally, evaluating the ungated waveforms may provide greater insight into facility reverberance and its associated interaction with the flow field. Understanding the causes of such deviation can provide bounds on, and possibly lead to improvements in, source analysis techniques such as microphone array signal processing.

ACKNOWLEDGMENTS

The author wishes to thank Dr. Florence V. Hutcheson for leading the plasma source efforts in the NASA Langley QFF and Mr. Daniel J. Stead for his work with test setup and data acquisition. He also wishes to acknowledge Dr. Russell Thomas for managing the overall task and NASA contribution to an international collaboration on noise shielding studies, of which this test was a part. Finally, he wishes to acknowledge internal funding by the NASA Advanced Air Transport Technology Project.

REFERENCES

[1] P. T. Soderman and C. S. Allen, "Microphone measurements in and out of airstream," in *Aeroacoustic Measurements*, edited by T. J. Mueller (Springer-Verlag, Berlin, Heidelberg, New York, 2002).

[2] J. P. Gomes, A. Bergmann, and H. Holthusen, "Aeroacoustic wind tunnel design," CEAS Aeronautical Journal **10**(1), 231–249 (2019) doi: https://doi.org/10.1007/s13272-019-00372-7.

[3] M. Szőke, C. J. Bahr, F. V. Hutcheson, and W. J. Devenport, "Characterization of Hybrid Wind Tunnel Environments using Laser-Induced Acoustic Sources," AIAA SciTech 2020 Forum, AIAA 2020-1253, Orlando, Florida (6–10 January 2020) doi: https://doi.org/10.2514/6.2020-1253.

[4] C. J. Bahr, F. V. Hutcheson, and D. J. Stead, "Unsteady Propagation and Mean Corrections in Open-Jet and Kevlar® Wind Tunnels," AIAA Journal **59**(11), 4598–4609 (2021) doi: https://doi.org/10.2514/1.J060469.

[5] K.-S. Rossignol, J. Delfs, and F. Boden, "On the Relevance of Convection Effects for a Laser-Generated Sound Source," 21st AIAA/CEAS Aeroacoustics Conference, AIAA 2015-

3146, Dallas, Texas (22–26 June 2015), doi: https://doi.org/10.2514/6.2015-3146.

[6]P. Gottlieb, "Sound Source near a Velocity Discontinuity," The Journal of the Acoustical Society of America **32**(9), 1117–1122 (1960) doi: https://doi.org/10.1121/1.1908361.

[7]R. K. Amiet, "Refraction of sound by a shear layer," Journal of Sound and Vibration **58**(4), 467–482 (1978) doi: https://doi.org/10.1016/0022-460X(78)90353-X.

[8]T. F. Balsa, "The far field of high frequency convected singularities in sheared flows, with an application to jet-noise prediction," Journal of Fluid Mechanics **74**(2), 193–208 (1976) doi: https://doi.org/10.1017/S0022112076001766.

[9]M. E. Goldstein, "High frequency sound emission from moving point multipole sources embedded in arbitrary transversely sheared mean flows," Journal of Sound and Vibration **80**(4), 499–522 (1982) doi: https://doi.org/10.1016/0022-460X(82)90495-3.

[10]R. H. Schlinker and R. K. Amiet, "Refraction and Scattering of Sound by a Shear Layer," NASA Contractor Report 3371 (1980) https://ntrs.nasa.gov/citations/19810008332.

[11]J. Jiao, J. W. Delfs, and J. Dierke, "Towards CAA based Acoustic Wind Tunnel Corrections for Realistic Shear Layers," 21st AIAA/CEAS Aeroacoustics Conference, AIAA 2015-3278, Dallas, Texas (22–26 June 2015) doi: https://doi.org/10.2514/6.2015-3278.

[12]J. W. Miles, "On the Reflection of Sound at an Interface of Relative Motion," The Journal of the Acoustical Society of America **29**(2), 226–228 (1957) doi: https://doi.org/10.1121/1.1908836.

[13]H. S. Ribner, "Reflection, Transmission, and Amplification of Sound by a Moving Medium," The Journal of the Acoustical Society of America **29**(4), 435–441 (1957) doi: https://doi.org/10.1121/1.1908918.

[14]V. Guillemin and S. Sternberg, *Geometric Asymptotics*, revised ed. (American Mathematical Society, 1990), Chapter 1.

[15]V. E. Ostashev and D. K. Wilson, *Acoustics in Moving Inhomogeneous Media*, 2nd ed. (CRC Press, 2016), Chapter 4.

[16]C. Bahr, N. S. Zawodny, T. Yardibi, F. Liu, D. Wetzel, B. Bertolucci, and L. Cattafesta, "Shear layer time-delay correction using a non-intrusive acoustic point source," International Journal of Aeroacoustics **10**(5 & 6) 497–530 (2011) doi: https://doi.org/10.1260/1475-472X.10.5-6.497.

[17]Q. Qin and K. Attenborough, "Characteristics and application of laser-generated acoustic shock waves in air," Applied Acoustics **65**(4), 325–340 (2004) doi: https://doi.org/10.1016/j.apacoust.2003.11.003.

[18]A. Chou, P. Balakumar, and S. P. Schneider, "Development of Instabilities Generated by Freestream Laser Perturbations in a Hypersonic Boundary Layer," AIAA Journal **55**(3), 799–807 (2017) doi: https://doi.org/10.2514/1.J055280.

[19]C. H. Liu and K. C. Yeh, "Pulse spreading and wandering in random media," Radio Science **14**(5), 925–931 (1979) doi: https://doi.org/10.1029/RS014i005p00925.

[20]V. E. Ostashev, D. K. Wilson, S. L. Collier, J. E. Cain, and S. Cheinet, "Cross-frequency coherence and pulse propagation in a turbulent atmosphere," The Journal of the Acoustical

Society of America **140**(1), 678–691 (2016) doi: https://doi.org/10.1121/1.4959003.

[21] "Method for calculation of the absorption of sound by the atmosphere," ANSI S1.26-1995 (ASA 113-1995), The Acoustical Society of America (1995).

[22] *Condenser Microphones and Microphone Preamplifiers for acoustic measurements* (Brüel & Kjær, 1982).

[23] C. Bahr, N. S. Zawodny, B. Bertolucci, K. Woolwine, F. Liu, J. Li, M. Sheplak, and L. Cattafesta, "Measurement of Phased Array Point Spread Functions for use with Beamforming," 17th AIAA/CEAS Aeroacoustics Conference, AIAA 2011-2767, Portland, Oregon (5–8 June 2011), doi: https://doi.org/10.2514/6.2011-2767.

[24] C. J. Bahr, N. S. Zawodny, B. Bertolucci, J. Li, M. Sheplak, and L. N. Cattafesta, "A plasma-based non-intrusive point source for acoustic beamforming applications," Journal of Sound and Vibration **344**, 59–80 (2015) doi: http://dx.doi.org/10.1016/j.jsv.2015.01.023.

[25] M. Szőke, C. Bahr, L. Cattafesta, K. S. Rossignol, H. Ura, Y. Zhang, and F. Zigunov, "Comparative Assessment of Sound Generated Using Laser-Induced Plasma," 3rd Hybrid Anechoic Wind Tunnel Workshop, AIAA AVIATION 2021 Forum, Virtual, (2–6 August 2021), https://ntrs.nasa.gov/citations/20210019172.